

Electron Precipitation Caused by Intense Whistler-Mode Waves: Combined Effects of Anomalous Scattering and Phase Bunching

- Longzhi Gan^{1*}, Wen Li¹, Miroslav Hanzelka¹, Oianli Ma^{1,2}, Jav M. Albert³, and Anton V. 1
- Artemyev⁴ 2
- ¹Center for Space Physics, Boston University, Boston, MA, United States 3
- ²Department of Atmospheric and Oceanic Sciences, University of California, Los Angeles, CA, 4
- 5 **United States**
- 6 ³Air Force Research Laboratory, Kirtland AFB, NM, United States
- ⁴Department of Earth, Planetary, and Space Sciences, University of California, Los Angeles, CA, 7
- 8 **United States**

- 10 * Correspondence:
- Longzhi Gan 11
- 12 lzgan@bu.edu
- 13 Keywords: nonlinear effects, wave-particle interaction, whistler-mode waves, electron
- precipitation, phase bunching, anomalous trapping. 14
- 15 **Abstract**
- 16 Resonant interactions with whistler-mode waves are a crucial mechanism that drives the precipitation
- 17 of energetic electrons. Using test particle simulations, we investigated the impact of nonlinear
- interactions of whistler-mode waves on electron precipitation across a broad energy range (10 keV-1 18
- 19 MeV). Specifically, we focused on the combined effects of phase bunching and anomalous
- 20 scattering, including anomalous trapping and positive bunching. It is shown that anomalous
- 21 scattering transports electrons away from the loss cone and the only process directly causing
- 22 precipitation in the nonlinear regime is the phase bunching. We further show that their combined
- 23
- effects result in a precipitation-to-trapped flux ratio lower than the quasilinear expectations in a
- 24 quasi-equilibrium state. Additionally, we calculated the diffusion and advection
- 25 coefficients associated with the nonlinear trapping and bunching processes, which are vital
- 26 for understanding the underlying mechanisms of the precipitation. Based on these coefficients, we
- characterized the phase bunching boundary, representing the innermost pitch angle boundary where 27
- phase bunching can occur. A further analysis revealed that electrons just outside this boundary, rather 28
- 29 than near the loss cone, are directly precipitated, while electrons within the boundary are prevented
- from precipitation due to anomalous scattering. Moreover, we demonstrated that the regime of 30
- 31 dominant nonlinear precipitation is determined by the combination of the phase bunching boundary
- 32 and the inhomogeneity ratio. This comprehensive analysis provides insights into the nonlinear effects
- 33 of whistler-mode waves on electron precipitation, which are essential for understanding physical
- 34 processes related to precipitation, such as microbursts, characterized by intense and bursty electron
- 35 precipitation.

61

1 Introduction

- 39 Electron precipitation into the Earth's upper atmosphere is a crucial process for the loss of energetic
- electrons in the radiation belts. Resonant interactions with whistler-mode waves play a significant 40
- 41 role in scattering electron pitch angles into the loss cone, resulting in efficient electron precipitation.
- For instance, the short and intense electron precipitation events, known as microbursts, are widely 42
- 43 attributed to be driven by whistler-mode chorus waves (Breneman et al., 2017; Chen et al., 2022;
- Miyoshi et al., 2020). These waves contribute to the depletion of the outer radiation belt (e.g., Blake 44
- et al., 1996; O'Brien et al., 2004; Thorne et al., 2005). Specifically, ~1 MeV (mega-electron-45
- volt) electrons can be precipitated through interactions with ducted chorus waves at high magnetic 46
- latitudes (Chen et al., 2022), while sub-MeV electrons are subject to resonances with chorus waves at 47
- 48 moderate magnetic latitudes (Douma et al., 2018; Shumko et al., 2018; Zhang et al., 2022).
- 49 Ouasilinear theory, which assumes diffusive resonant interactions between electrons and whistler-
- 50 mode waves (Kennel & Engelmann, 1966; Lyons, 1974), is commonly employed in
- 51 modeling interactions between electrons and whistler-mode waves. It has been successful in
- simulating long-term energetic electron dynamics associated with whistler-mode waves (e.g., Albert 52
- et al., 2009; Horne et al., 2005; Li et al., 2014; Ma et al., 2018; Thorne et al., 2013). However, recent 53
- 54 observations have revealed that whistler-mode waves can often possess sufficient intensity to
- 55 drive nonlinear interactions with energetic electrons (Zhang et al., 2018, 2019). Comparisons
- between numerical and observational results have also shown that quasilinear theory (Kennel & 56
- 57 Engelmann, 1966) alone is inadequate to explain the intense electron precipitation
- 58 observed at both low Earth orbit (Mozer et al., 2018) and in the near-equatorial region (Shumko et
- al., 2018). Hence, it is believed that nonlinear interactions between electrons and whistler-mode 59 60
 - waves play a significant role in these processes.

62 Nonlinear interactions between electrons and whistler-mode waves typically involve two main

- 63 mechanisms: nonlinear phase trapping and phase bunching (Bortnik et al., 2008). In the case of phase
- 64 trapping, electrons become trapped in resonance with whistler-mode waves and are rapidly
- accelerated to higher energies and larger pitch angles (Albert, 2000; Artemyev et al., 2014; Omura et 65
- al., 2007; Vainchtein et al., 2018). On the other hand, phase bunching scatters electrons to lower 66
- energies and smaller pitch angles (Albert, 1993; Artemyev et al., 2018), which is believed to drive 67
- the intense electron precipitation. Recent studies have also highlighted additional nonlinear effects, 68
- 69 namely anomalous trapping (Kitahara & Katoh, 2019) and positive bunching (Gan et al., 2020).
- 70 Both anomalous trapping and positive bunching occur for electrons with small equatorial pitch
- angles. Anomalous trapping can efficiently accelerates electrons to higher energies and pitch angles, 71
- similar to standard phase trapping. However, electrons "anomalously" trapped at small pitch 72
- 73 angles exhibit a much larger ratio of trapped electrons compared to the entire electron population,
- 74 as compared to phase trapping. Positive bunching electrons, on the other hand, undergo the
- process similar to phase bunching but in the opposite direction. While phase bunching always 75
- 76 decreases electron pitch angle and energy, positive bunching increases the pitch angles and energies
- of electrons with small pitch angles. The theoretical analysis of these two processes was conducted 77
- in earlier studies by Neishtadt (1975) and Henrard & Lemaitre (1983), as well as a more 78
- 79 recent study by Bellan (2013), by utilizing the Hamiltonian approach. Building upon these previous
- studies, Albert et al. (2021) and Artemyev et al. (2021) discussed the anomalous trapping process 80
- specifically in the context of interactions between electrons and whistler-mode 81

- 82 waves, providing theoretical criteria for the occurrence of anomalous trapping. Later in this paper,
- 83 these criteria are examined in detail and compared to numerical results.
- Previously, it was believed that intense electron precipitation events were associated with nonlinear 84
- interactions. However, electrons near the loss cone experience anomalous trapping and positive 85
- 86 bunching, collectively referred to as anomalous scattering (AS) from now on. Anomalous scattering
- 87 always increases electron pitch angles, which reduces precipitation. Conversely, phase
- 88 bunching can transport electrons non-locally into the loss cone in phase
- 89 space, thereby increasing precipitation. The combined effects of anomalous scattering and phase
- 90 bunching on electron precipitation represent a key question in understanding nonlinear electron
- precipitation caused by whistler-mode waves, which remains unanswered. Anomalous scattering can 91
- 92 also occur when electrons interact with electromagnetic ion cyclotron (EMIC) waves. Grach and
- 93 Demekhov (2020) showed that nonlinear interactions with parallel and intense EMIC waves lead to a
- 94 higher level of loss cone filling near the minimum resonance energy. Bortnik et al. (2022)
- 95 specifically discussed the effects of anomalous scattering, referred to as force bunching, and
- 96 concluded that force bunching could potentially block electron precipitation caused by EMIC
- 97 waves. Subsequently, Grach et al. (2022) and Hanzelka et al. (2023) evaluated the effects of force
- 98 bunching on the precipitation phase space density (PSD) and demonstrated that force bunching does
- 99 not reduce the precipitation PSD. This is because the electrons scattered outward are balanced by the
- 100 inward transport of electrons within the loss cone.
- 101 In this paper, we address the question of the combined effects of anomalous scattering and phase
- 102 bunching by parallel whistler-mode waves. Such effects have been discussed for EMIC waves, as
- 103 introduced above, but not for the case of whistler-mode waves. We use test particle simulations to
- 104 numerically evaluate the nonlinear interactions. Quasilinear theory and nonlinear Hamiltonian
- 105 approaches are also compared to numerical results. Section 2 describes the numerical methodology
- 106 including test particle and quasilinear methods. Section 3 describes the main results of this paper.
- Section 4 discusses the implications of our results and summarizes the main conclusions. 107

109 2 Methodology

108

110

2.1 **Test Particle Simulation**

- 111 This paper uses the test particle simulations to model the interactions between electrons and whistler-
- 112 mode waves, following the method of Gan et al. (2020). In this study, a 1-D dipole geometry is
- employed for the background magnetic field, with the equatorial field intensity equivalent to that at L 113
- 114
- = 6. The cold electron density follows an empirical density model, $n_e(\lambda) = n_e^{eq} \cos^{-4} \lambda$ (Denton et al., 2004), where $n_e^{eq} = 5 \text{ cm}^{-3}$ is the equatorial electron density. The upper atmosphere boundary is set at an altitude of 100 km, where electrons are considered lost. All whistler-mode waves are 115
- 116
- 117 released from the equator and propagate with wave normal angle of 0° to both hemispheres up to
- 118
- magnetic latitude of 30°. The whistler-mode wave frequency is set to 0.3 f_{ce}^{eq} for all simulations, where f_{ce}^{eq} is the equatorial electron gyrofrequency. The latitudinal distribution of wave amplitude 119
- follows $B_w(\lambda_{deg}) = B_w^0 \tanh(\lambda_{eq}) \tanh(30^\circ \lambda_{eq})$. Here B_w^0 is the wave amplitude of choice for 120
- each simulation, which is assumed to be uniform versus time, and λ_{deg} is the magnetic latitude 121
- measured in unit of degrees. Initial electron energy ranges from 10 keV to 1 MeV, with 20 energy 122
- 123 bins uniformly distributed in logarithmic space.

- 124 Initial electron equatorial pitch angle ranges from 0° to 90°, with 360 uniform bins. For simulations
- of electron PSD distribution, electrons are released with 90 uniform bins of gyro-phase from 0° to
- 126 360°, and 30 uniform bins of magnetic latitudes between the two mirror points. Initial electron PSD
- distribution is:

128
$$f(\alpha_{eq}, E) = \begin{cases} j(E) \sin \alpha_{eq} & \alpha_{eq} > \alpha_{lc} \\ 0 & \alpha_{eq} \le \alpha_{lc} \end{cases}$$
 (1)

$$j(E) = 10^{11.45 - 3.11 \log_{10}(E)}$$
 (2)

- Here, α_{eq} is the equatorial pitch angle, α_{lc} is the loss cone calculated at the equator, and E is the
- electron energy in keV. This distribution is calculated based on the time averaged electron flux
- measured by Van Allen Probe A during the time interval of 19:40:00 to 20:10:00 UT on January 20th,
- 2016, during a microburst conjunction event reported in Breneman et al. (2017). The full initial PSD
- distribution in pitch angle-energy space is shown in Figure 2A. The fitting of the Van Allen Probe
- measurements is shown in Figure S1 in the Supplementary Material. For simulations calculating the
- electron diffusion and advection coefficients, 360 electrons are released from the equator with initial
- gyro-phase uniformly distributed between 0° and 360° within each pitch angle-energy bin. The
- calculation of diffusion and advection coefficients for different resonant interactions is discussed in
- more detail in Section 3.3.

2.2 Quasilinear Theory and Quasi-Equilibrium State (QES) of Electron Precipitation

- 141 Test particle simulation results are quantitatively compared to quasilinear results. Quasilinear
- diffusion coefficients are calculated based on Ma et al. (2018), using the same background and wave
- parameters, as described in Section 2.1. Electron PSD distribution near the loss cone at the quasi-
- equilibrium state is calculated following Kennel & Petschek (1966):

$$J_{in}(\alpha_{eq,in}, E) = \frac{S(E)}{D^*} \left\{ \frac{I_0\left(\frac{\alpha_{eq,in}}{\alpha_{lc}} z_0\right)}{z_0 I_1(z_0)} \right\}$$
(3)

$$J_{out}(\alpha_{eq,out}, E) = \frac{S(E)}{D^*} \left\{ \frac{I_0(z_0)}{z_0 I_1(z_0)} + \ln\left(\frac{\sin\alpha_{eq,out}}{\sin\alpha_{lc}}\right) \right\}$$
(4)

- Here S(E) is the rate of electrons entering the loss cone, $z_0 = \frac{\alpha_{lc}}{\sqrt{D^*\tau}}$, $D^* \approx D_{\alpha\alpha}|_{\alpha = \alpha_{lc}} \times \cos{(\alpha_{lc})}$,
- 148 $D_{\alpha\alpha}|_{\alpha=\alpha_{lc}}$ is the pitch angle diffusion coefficient at the equatorial loss cone α_{lc} , $\alpha_{eq,in}$ and $\alpha_{eq,out}$ are
- the equatorial pitch angles inside and outside the loss cone, respectively, E is the electron energy, τ is
- a quarter of the electron bounce period, and I_0 and I_1 are the modified Bessel functions. Electron
- precipitation flux ratio, which is the ratio of precipitation to trapped flux, is calculated based on
- 152 Equation (3) and (4).

153
$$\chi(E) = \frac{\frac{1}{\alpha_{lc}} \int_0^{\alpha_{lc}} J_{in} sin\alpha d\alpha}{\frac{1}{\alpha_{sc} - \alpha_{lc}} \int_{\alpha_{lc}}^{\alpha_{sc}} J_{out} sin\alpha d\alpha}$$
 (5)

- Here, $\alpha_{sc} = \arcsin\left(\sqrt{\frac{B_{eq}}{B_{sc}}}\right)$, where B_{eq} is the Earth's equatorial dipole magnetic field intensity at L
- shell of 6, and B_{sc} is the field intensity at magnetic latitude of 64.72° at the same L shell, which
- 156 corresponds to an altitude of 600 km. This is the altitude of the FIREBIRD (Focused Investigations
- of Relativistic Electron Burst Intensity, Range, and Dynamics) CubeSat as reported in Breneman et
- al. (2017). Equation (5) is set to mimic the flux ratio one would observe by a typical LEO CubeSat.
- The precipitation flux ratio from test particle simulations is also calculated using Equation (5).

2.3 Identification of Phase Trapping Electrons

- To quantify the contribution of different nonlinear processes, we identify the electrons that are phase
- trapped or anomalously trapped during simulations of half bounce-period. The key characteristic of
- nonlinearly trapped electrons is that they stay in resonance with whistler-mode waves for an
- 164 extensive amount of time. The resonance is identified by calculating the relative phase speed $\dot{\zeta} =$
- $d\zeta/dt$, where ζ is the phase angle between the electron perpendicular velocity and the wave
- magnetic field vector (for detailed definition of ζ , see Tao & Bortnik (2010)). $\dot{\zeta} = 0$ marks the
- moment when an electron is in resonance with whistler-mode waves. Electrons that cross the
- resonance line for more than n=5 times are identified as the phase/anomalous trapping electrons. The
- criterion of 5 is arbitrarily selected to exclude any electrons that are detrapped quickly.

3 Results

160

170

171

3.1 Electron Precipitation in Nonlinear Regime

- Figure 1 illustrates the typical trajectories of electrons interacting with intense whistler-mode
- waves of 1 nT, which represents typical nonlinear interactions. In Figures 1A-1B, 360
- electrons initially with an energy of 50 keV and an equatorial pitch angle of 10° move
- 175 from the mirror point to the equator. All of these electrons experience anomalous trapping, leading to
- a significant increase in their pitch angles and energies. In this particular case, none of the electrons
- are precipitated, but their pitch angles increase due to the nonlinear interactions. Electrons with the
- same energy, but smaller pitch angles also undergo anomalous trapping, preventing
- any electrons close to the loss cone from being precipitated in the typical nonlinear regime. For
- electrons with the same energy (50 keV) but slightly larger pitch angles (13.5°), the probability
- of anomalous trapping decreases, as shown in Figures 1C-1D. The non-trapping
- electrons experience positive bunching (Gan et al., 2020), which also leads to an increase in
- their pitch angles. Consequently, all electrons in this scenario are further affected by the anomalous
- scattering, resulting in no precipitation. When the pitch angles are even higher (18°),
- electrons exhibit the typical nonlinear phase trapping and phase bunching features. Figures 1E-1F
- demonstrate that phase trapping increases the electron pitch angle and energy, while phase bunching
- decreases them. In this case, phase bunching scatters electrons into the loss
- cone, driving precipitation. The typical nonlinear interactions depicted in Figure 1 indicate that
- electron precipitation in the nonlinear regime is primarily driven by phase
- bunching, which only occurs when the equatorial pitch angle is sufficiently large, surpassing the
- pitch angle range considered in the quasilinear theory.

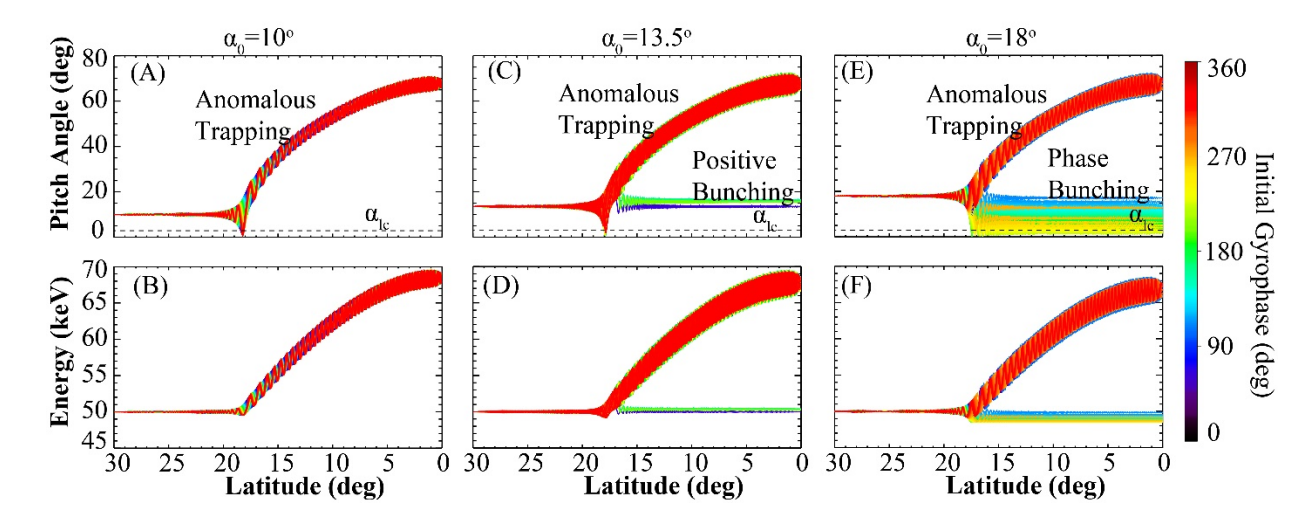


Figure 1. Typical interactions between electrons ($E_k = 50 \ keV$) and intense whistler-mode waves ($B_w = 1 \ nT$). (A) Pitch angle variation versus magnetic latitude of electrons with an initial equatorial pitch angle of 10° , undergoing anomalous trapping, color coded for different initial gyro-phases; (B) energy variation of the same electrons as those in (A); (C-D) same as (A-B) but for electrons with an initial equatorial pitch angle of 13.5° , undergoing anomalous trapping and positive bunching; (E-F) same as (A-B) but for electrons with an initial equatorial pitch angle of 18° , undergoing phase trapping and phase bunching. The horizontal black dashed lines mark the equatorial loss cone. Note that only interactions in panels (E-F) lead to electron precipitation.

To assess the combined effects of various nonlinear processes on electron precipitation, we conducted three sets of test particle simulations lasting for 20 seconds each. These simulations employed three different wave amplitudes: 50 pT, 200 pT, and 1 nT. All models shared the same initial PSD distribution, described by Equations (1) & (2) and displayed in Figure 2A. The PSD evolution of the precipitating electrons is illustrated in Figure 2B (Nunn & Omura, 2015), with colors representing different energies. Dashed, dotted, and solid lines correspond to wave amplitudes of 50 pT, 200 pT, and 1 nT, respectively. A common characteristic observed in all models and energy ranges is the significant variability of precipitating electron PSD during the initial few seconds of the simulations. However, it tends to stabilize within 20 s, indicating the quasi-equilibrium state. In this state, the overall shapes of the electron PSD distributions in pitch angle and energy change slowly and can be considered stable. This paper will primarily focus on discussing the QES derived from the test particle simulations and comparing it to the results obtained from the quasilinear approach. It is important to note that the precipitation PSD in the QES is lower than that observed within the first 1-2 s. Consequently, some of the conclusions drawn from the OES may not be applicable to events observed on timescales shorter than approximately 1 s, such as microbursts (Zhang et al., 2022).

Based on the evolution of the precipitation PSD presented in Figure 2B, we extracted a snapshot of the electron PSD at a simulation time of 20 s and compared it to the expected QES based on the calculations from quasilinear theory (Equations (3) and (4)). The results are displayed in Figures 2C, 2D, and 2E for wave amplitudes of 50 pT, 200 pT, and 1 nT, respectively, with colors indicating different energy levels. The corresponding dotted lines represent the quasilinear results. As depicted in Figure 2C, for a wave amplitude of 50 pT, the test particle results align well with the quasilinear results, except for deep within the loss cone at low energies. The lack of electrons deep within the loss cone is attributed to the method used for setting the atmosphere boundary in test particle simulations, which does not include any backscattering processes.

This demonstrates the applicability of quasilinear models when the wave amplitude is not sufficiently intense to induce nonlinear interactions. For an amplitude of 200 pT, the test particle results match the quasilinear predictions for energies above approximately 50 keV. However, at lower energies, the test particle PSD is lower than the quasilinear results within the loss cone. Additionally, the test particle results exhibit a similar shape in the PSD distribution within the loss cone. For a wave amplitude of 1 nT, similar PSD distributions are observed for all energy levels, and they are consistently smaller than the quasilinear expectations. The outcomes depicted in Figures 2D and 2E highlight that nonlinear interactions generate comparable PSD pitch angle distributions for different energy levels within the loss cone, all of which are lower than the quasilinear expectations. The specific nonlinear processes driving these observed features are analyzed in Section 3.2.

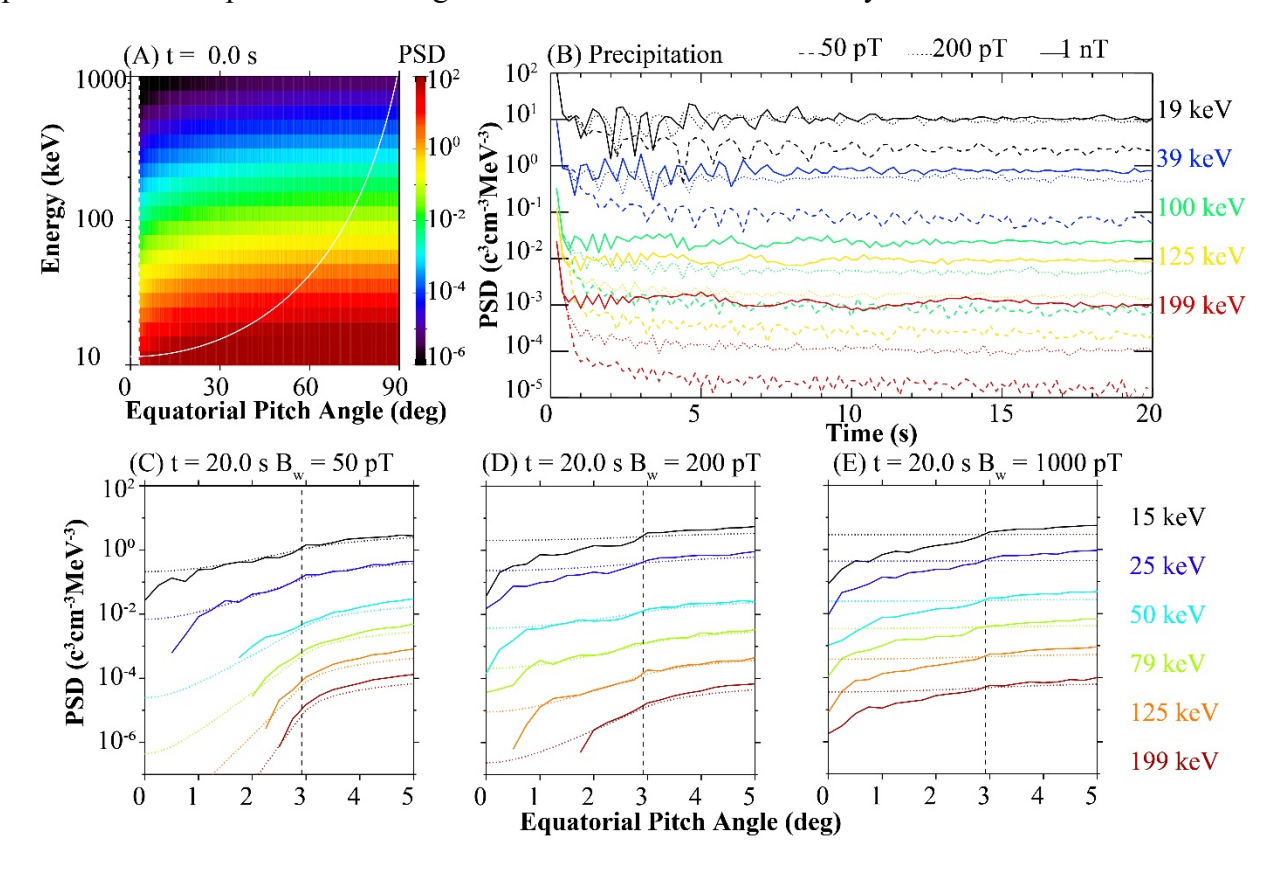


Figure 2. The PSD evolution of the precipitating electrons driven by whistler-mode waves with different wave amplitudes. (A) Initial PSD distribution in equatorial pitch angle-energy space. The vertical black dashed line marks the loss cone. The white solid line marks the minimum resonant energy. (B) Precipitation PSD variation versus time, color coded for different energies. Dashed, dotted, and solid lines represent the model results using whistler-mode amplitude of 50 pT, 200 pT, and 1 nT, respectively. (C-E) Pitch angle distribution of electron PSD near the loss cone after 20 s of simulations using wave amplitude of 50 pT, 200 pT, and 1 nT, respectively, color coded for different energies. The loss cone is marked by the vertical dashed lines. The dotted lines are the results calculated with quasilinear methods.

3.2 Nonlinear Processes Driving Electron Precipitation

To investigate the specific nonlinear processes driving electron precipitation, we tracked the electrons that were precipitated at time $t_1 = 20 \, s$. Their PSD distributions in the equatorial pitch angle-energy space at different times t_0 are illustrated in Figure 3. Figures 3A and 3B display the tracing results for

250 models using a wave amplitude of 200 pT at t_0 of 19.8 s and 19 s, respectively. The typical quarter-251 bounce period of electrons is about 0.3 s (energy of 100 keV and pitch angle of 5°). For a whistler-252 mode wave with a fixed single frequency, electrons can only resonate with the wave once during one 253 quarter-bounce period. Thus, the two timesteps illustrated the precipitation effects of 1 ($t_0 = 19.8 \text{ s}$) to about 3 cyclotron resonant interactions ($t_0 = 19.0 \text{ s}$) with whistler-mode waves. In both cases, sources 254 255 located away from the loss cone contribute to the precipitation PSD for energies below 30 256 keV, where PSD distributions of nonlinear characteristics were observed in Figure 2D. These source 257 electrons are transported into the loss cone by the nonlinear phase bunching processes since diffusive 258 processes cannot transport electrons nonlocally in just 1-3 cyclotron resonances. A diffusive 259 precipitation mechanism would also result in a continuous PSD distribution, while discrete 260 distributions are shown in Figure 3. Specifically, for an amplitude of 1 nT, the contribution of phase 261 bunching electrons is dominant due to the dominant nonlinear anomalous scattering and phase 262 bunching effects. For the case of 200 pT, both diffusive scattering and phase bunching contribute to 263 precipitation, as denoted by the two initial PSD distributions separated by a gap (Figures 3A-3B). 264 The gaps of PSD distribution are exhibited for both cases of 200 pT and 1 nT. These gaps arise due to the presence of anomalous scattering, which transport electrons to sufficiently large pitch angles 265 266 and prevent them from precipitation. This pattern, observed in Figures 3A and 3B, is more 267 pronounced when the wave amplitude is 1 nT by crossing the entire resonant energy range, as shown 268 in Figures 3C and 3D. In this scenario, anomalous scattering dominates a significant range of pitch 269 angle and energy, resulting in the substantial gaps illustrated in Figures 3C and 3D. Moreover, the 270 advection effects of nonlinear phase bunching are evident in Figure 3C, as they transport electrons 271 into the loss cone from pitch angles as large as 30° within a time span of 0.2 s. The outer pitch angle 272 boundary of the gaps, which corresponds to the inner boundary of the phase bunching source, 273 converges to smaller pitch angles as the energy increases. This observation aligns with the theoretical 274 predictions presented by Albert et al. (2021) and Artemyev et al. (2021). The tracing results in Figure 275 3 demonstrate that anomalous scattering plays a prominent role at lower energies and larger wave 276 amplitudes, effectively preventing a majority of electrons from undergoing precipitation, as indicated 277 by the gap right outside of the loss cone in Figure 3. The pitch angle range of the gaps resulting from 278 these two nonlinear processes can extend up to 20° (30°) for wave amplitudes of 200 pT (1 nT). The only mechanism directly driving precipitation in the nonlinear regime is phase bunching. 279

We further confirm this mechanism we propose, by comparing the tracing results with the theoretical analysis by Albert et al. (2021) and Artemyev et al. (2021). For anomalous trapping to occur, Albert et al. (2021) provides the criterion $\delta < 0$, where

283
$$\delta = \frac{2}{3} \frac{\eta^2 \left(1 - \frac{1}{\eta^2}\right)^{\frac{2}{3}}}{\left(\frac{B_w}{B_0}\right)^{\frac{2}{3}}} \frac{\omega}{\Omega_c} I_{res} - 1.$$
 (6)

Here, η is the refractive index, B_w is the wave amplitude, B_0 is the background magnetic field, ω is the wave frequency, Ω_c is the electron gyrofrequency, and I_{res} is the resonant value of action I (for the full definition see Equation (5) in Albert et al. (2021)). Similarly, Artemyev et al. (2021) provides the criterion for anomalous trapping as $y_R < 1$, where

$$y_{R} = \frac{2}{3} \frac{\kappa^{\frac{2}{3}} k^{2} c^{2}}{\gamma_{0}^{\frac{4}{3}} \Omega_{c}^{2}} \frac{I_{R} \Omega_{c}}{m_{e} c^{2} \left(\frac{B_{w}}{B}\right)^{\frac{2}{3}}}.$$
 (7)

Here, $\kappa = \gamma_0^2 - \left(\frac{\Omega_c}{kc} + \sqrt{\gamma_0^2 - 1}\right)^2$, γ_0 is the Lorentz factor of electrons, k is the wave vector, c is the speed of light, and I_R is the resonant value of action I (for full definition see Equation (6) in Artemyev et al. (2021)). δ and y_R are equivalent parameters only in a slightly different format. For completeness, we show both parameters here. $\delta = 0$ and $y_R = 1$ are plotted in Figure 3 with solid and dashed lines, respectively. As is shown in Figure 3, the outer boundary of the gap qualitatively agrees with the theoretical boundaries. This confirms our proposed mechanism that the gap is due to nonlinear anomalous scattering. Note that the agreement between the test particle result and the theoretical boundaries is better for the amplitude of 1 nT than 200 pT. This is because the theoretical analysis is focused on the anomalous trapping while the positive bunching is not included, and the anomalous trapping probability is much larger for 1 nT. We will discuss the comparison with theoretical results in more detail in Section 3.3.

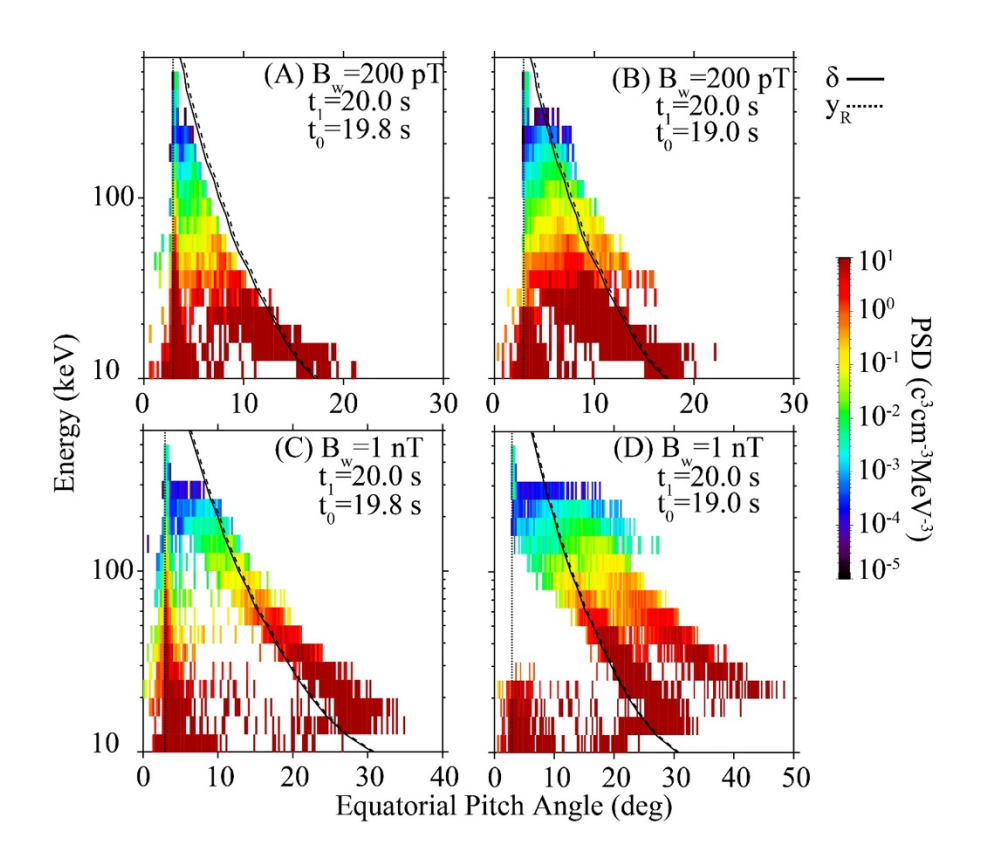


Figure 3. PSD distribution of precipitated electrons at time t_0 , with t_1 being the time of precipitation. (A) PSD distribution at 19.8 s with an amplitude of 200 pT; (B) PSD distribution at 19 s with an amplitude of 200 pT; (C-D) same as (A-B) but with an amplitude of 1 nT. The solid and dashed black lines are contours of $\delta = 0$ and $y_R = 1$, respectively, depicting the theoretical boundary of anomalous trapping.

307 Based on the analysis presented above, we discuss the mechanisms governing electron 308 precipitation in the presence of nonlinear interactions. Figure 4B provides an illustration of the pitch angle-energy space, where the phase bunching boundary is depicted. This boundary represents the 309 inner limit within which phase bunching can occur, transporting electrons toward the vicinity of the 310 311 loss cone. The advection and diffusion effects associated with the phase bunching process determine whether the electrons move into or out of the loss cone. For equatorial pitch angles smaller 312 313 than the phase bunching boundary values, the dominant effect of anomalous 314 scattering causes electrons to scatter into higher pitch angles. Consequently, electrons within the 315 phase bunching boundary cannot undergo direct precipitation through nonlinear interactions with 316 whistler-mode waves. However, once they are transported outside of this boundary, 317 they undergo precipitation through the phase bunching process. Furthermore, the phase bunching 318 boundary converges to smaller pitch angles as the energy increases, as indicated by the values $\delta = 0$ 319 and $y_R = 1$ in Figure 3.

We further quantify the precipitation in the nonlinear regime by calculating the precipitation flux ratio and comparing it to the quasilinear QES expectations defined in Equation (5). The comparison is presented in Figure 4A, where solid lines represent the test particle results and dashed lines represent the quasilinear results. Different colors correspond to different wave amplitudes. In the quasilinear regime, the test particle flux ratio aligns well with the quasilinear results, as demonstrated by the black lines representing an amplitude of 50 pT. For an amplitude of 1 nT, the quasilinear theory predicts a completely filled loss cone for all resonant energies. However, the test particle simulations, which are dominated by nonlinear processes across the entire energy range, yield a smaller flux ratio compared to the quasilinear theory. For an amplitude of 200 pT, nonlinear processes dominate the precipitation for energies below approximately 30 keV, as evidenced by the results in Figures 3A and 3B, which were discussed earlier. Consistently, Figure 4A illustrates that the test particle flux ratio is smaller than the quasilinear results below approximately 30 keV. However, for higher energies, the test particle results closely match the quasilinear ones, indicating that quasilinear processes are the main driving mechanism for electron precipitation in that energy range. Overall, the results suggest that nonlinear precipitation leads to a flux ratio smaller than that predicted by quasilinear expectations.

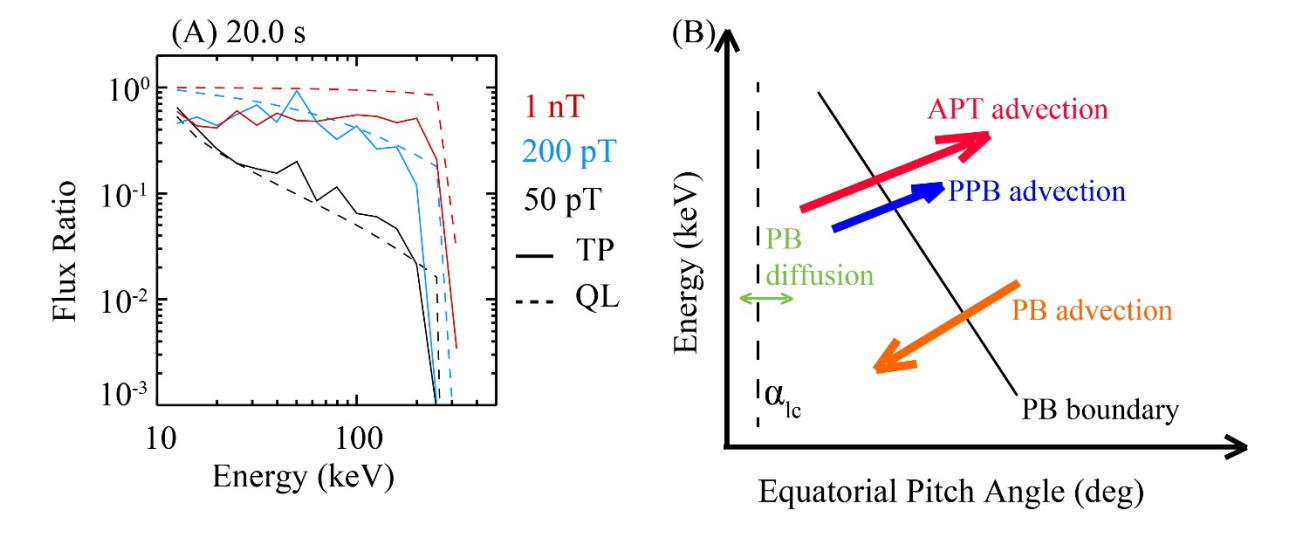


Figure 4. (A) Precipitation to trapped electron flux ratio versus energy, color coded for different wave amplitudes. The dashed lines mark the quasilinear results, and the solid lines represent the test particle results. (B) Illustration of electron precipitation mechanisms in the pitch angle and energy

320

321

322323

324

325

326

327

328

329

330

331

332333

334

335

336

337338

340 space in the nonlinear regime. Here, APT represents Anomalous Phase Trapping; PPB represents

Positive Phase Bunching; PB represents Phase Bunching. 341

Nonlinear Diffusion and Advection

342

343 As is shown in Figure 4A, electron precipitation in the nonlinear regime is driven by the combination 344 of various nonlinear processes. Thus, quantification of the nonlinear diffusion and advection is 345 critical for the understanding of nonlinear precipitation processes. Figure 5 shows the diffusion 346 coefficients based on quasilinear theory and test particle simulations for nonlinear waves (200 pT and 347 1 nT). The bounce-averaged quasilinear coefficients are calculated based on Ma et al. (2018), and are shown in Figures 5A & 5D for amplitudes of 200 pT and 1 nT, respectively. Quasilinear diffusion 348 coefficients at the equatorial loss cone $(D_{\alpha\alpha}|_{\alpha=\alpha_{lc}})$ are used to calculate the flux ratio in Figure 4A 349 350 following Equation (5). As is shown in both panels, $D_{\alpha\alpha}|_{\alpha=\alpha_{lc}}$ decreases with increasing energy.

 $D_{\alpha\alpha}|_{\alpha=\alpha_{lc}}$ with the amplitude of 1 nT (Figure 5D) is also much larger than that with the amplitude of 351

200 pT (Figure 5A), since $D_{\alpha\alpha} \propto B_w^2$. Diffusion coefficients calculated using test particle simulations are shown in Figures 5B & 5E. The test particle diffusion coefficients $D_{\alpha\alpha}$ are: 352

353

$$D_{\alpha\alpha}^{TP} = \frac{1}{2\tau} \overline{\left(\alpha_{eq} - \overline{\alpha_{eq}}\right)^2} \tag{8}$$

Here, au is a quarter of electron bounce period, $lpha_{eq}$ is the electron equatorial pitch angle. For the 355 356 amplitude of 200 pT, test particle diffusion coefficients show a similar range of values compared to 357 the quasilinear results, but with a different distribution. The peak diffusion values are distributed in 358 the middle of the resonant region (Figure 5B), instead of being near the minimum resonant energy 359 (Figure 5A). Two sharp transition boundaries correspond to the maximum diffusion coefficients in 360 Figure 5B. One is at the region of low energy and small pitch angle, extending from pitch angle near the loss cone and energy of ~30 keV to pitch angle of ~15° and energy of ~15 keV, which is at 361 minimum resonant energy boundary. This boundary marks the phase bunching boundary defined in 362 Figure 4B. The solid and dashed lines represent the theoretical boundaries from Albert et al. (2021) 363 364 and Artemyev et al. (2021), as is shown above in Figure 3. Similar to the conclusions in Section 3.2, 365 the theoretical boundaries agree with numerical phase bunching boundary qualitatively but show a 366 small offset in pitch angle. For regions to the left of the boundary, diffusion coefficients from test 367 particle simulations are much smaller than quasilinear results. This is because anomalous trapping is 368 dominant for this region, and trapping processes result in only advection without diffusion. The other 369 sharp transition boundary extends from pitch angles near the loss cone and energy of ~30 keV to 370 pitch angle of ~45° and energy of 500 keV. This is the nonlinear boundary, i.e., the boundary 371 between nonlinear and quasilinear regimes. Electrons to the left of this boundary interact with 372 whistler-mode waves through quasilinear processes, which shows a similar diffusion coefficient 373 distribution as the quasilinear results shown in Figure 5A. For the amplitude of 1 nT, only one of 374 these two sharp boundaries exists, specifically the phase bunching boundary. This is because nonlinear interactions are dominant for the entire resonant region, and thus the nonlinear boundary 375 376 disappeared. The theoretical bunching boundaries, also shown by solid and dashed lines, agree with 377 the numerical boundary better compared to the case of 200 pT. The maximum diffusion coefficients 378 shown in both Figures 5B & 5C are located at the upper nonlinear or resonant boundaries. Such 379 distributions are due to the strong modulation of diffusion coefficients caused by the nonlinear phase 380 trapping, which is most significant when the resonant latitude is largest (Gan et al., 2020). However, 381 as is shown in Section 3.2, phase bunching is the only process that directly precipitates electrons into 382 the nonlinear regime. Thus, we calculate the diffusion coefficients specifically for phase bunching

electrons by excluding the modulation from phase trapping in the nonlinear regime. The phase bunching diffusion coefficients are calculated following the equation below:

$$D_{\alpha\alpha}^{PB} = \frac{1}{2\tau} \overline{\left(\alpha_{eq}^{PB} - \overline{\alpha_{eq}^{PB}}\right)^2} \tag{9}$$

The parameters are the same as those of Equation (8) but for phase bunching electrons only. The phase bunching electrons are identified by excluding the phase trapping electrons. Identification of phase trapping is described in Section 2.3. $D_{\alpha\alpha}^{PB}$ for amplitudes of 200 pT and 1 nT are shown in Figures 5C and 5F, respectively. Phase bunching diffusion coefficients are much smaller than the diffusion coefficients calculated from quasilinear theory or from all electron populations in the test particle simulations. This simulation result confirms the previous theoretical analysis as shown in Figure 8 of Frantsuzov et al. (2023). For the amplitude of 200 pT (Figure 5C), phase bunching diffusion coefficients are only distributed in the region below the nonlinear boundary. This is because phase bunching only exists within this nonlinear regime. The maximum phase bunching diffusion coefficients are distributed close to the two boundaries defined above. For the amplitude of 1 nT, phase bunching diffusion coefficients are distributed to the right of the phase bunching boundary since anomalous trapping dominates the region to the right. The maximum diffusion coefficients for the amplitude of 1 nT is also located close to the phase bunching boundary.

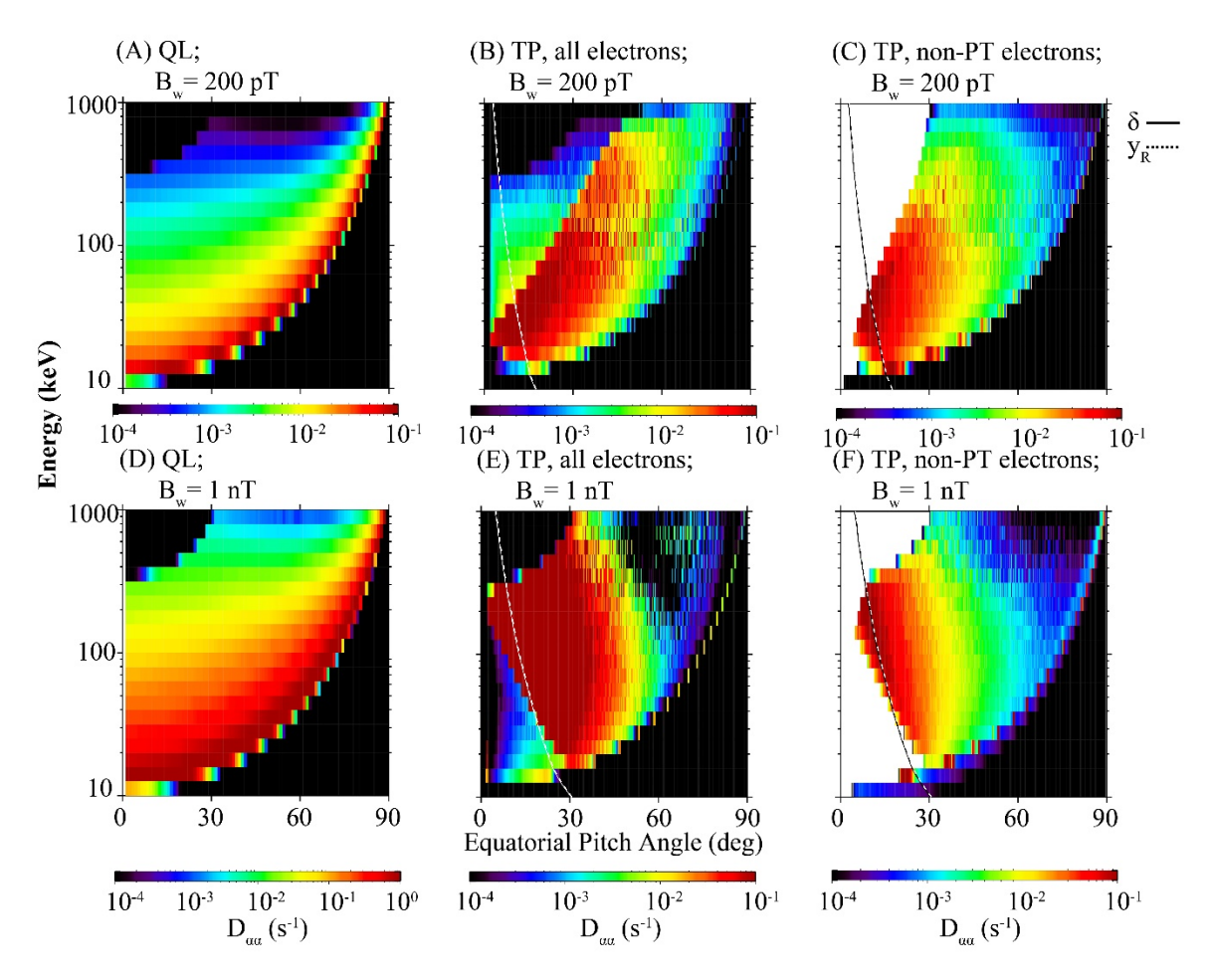


Figure 5. Diffusion coefficients of different electron populations and wave amplitudes, within the equatorial pitch angle-energy space. (A) Quasilinear diffusion coefficients; (B) diffusion coefficients of all electrons from test particle simulations; (C) diffusion coefficients of phase bunching electrons

for the amplitude of 200 pT from test particle simulations. (D-F) same as (A-C) but for the amplitude of 1 nT. The solid and dashed white lines are contours of $\delta = 0$ and $y_R = 1$, respectively.

403

404

405 406

407

408

409

410

411

412 413

414

415

416

417

418

419

420

421

422

423

424

425 426

427

428

Advection coefficients and the ratio of phase/anomalous trapping electrons are presented in Figure 6. Results for the amplitude of 200 pT and 1nT are shown in Figures 6A-6C, and Figures 6D-6F, respectively. As is shown in Figure 6A, phase trapping ratio, i.e., the ratio between the number of phase trapping electrons and the total population, is highest to the left of the phase bunching boundary, which reaches a value of 50%. Phase trapping advection is shown in Figure 6B, which is quantified by the average of equatorial pitch angle variation of the phase trapping electrons. Phase trapping advection is highest at the nonlinear boundary. Advection of the phase bunching is also denoted by the average of equatorial pitch angles for the phase bunching electrons. For small pitch angle region, phase bunching advection is positive due to dominant positive bunching processes, as shown in Figure 1B. The boundary of the positive advection agrees with the theoretical boundaries qualitatively well. Regarding the results for the amplitude of 1 nT (Figures 6D-6F), anomalous trapping probability reaches 100% within the phase bunching boundary. Phase trapping advection shows a similar distribution to that of 200 pT, with the highest advection at the upper resonant energy boundary, which corresponds to the highest resonant latitude. For advection of bunching electrons, positive bunching only occurs for pitch angles close to the phase bunching boundary with high energy. It is worth noting that the bunching processes are not possible for most regions left of the phase bunching boundary, due to the 100% trapping ratio.

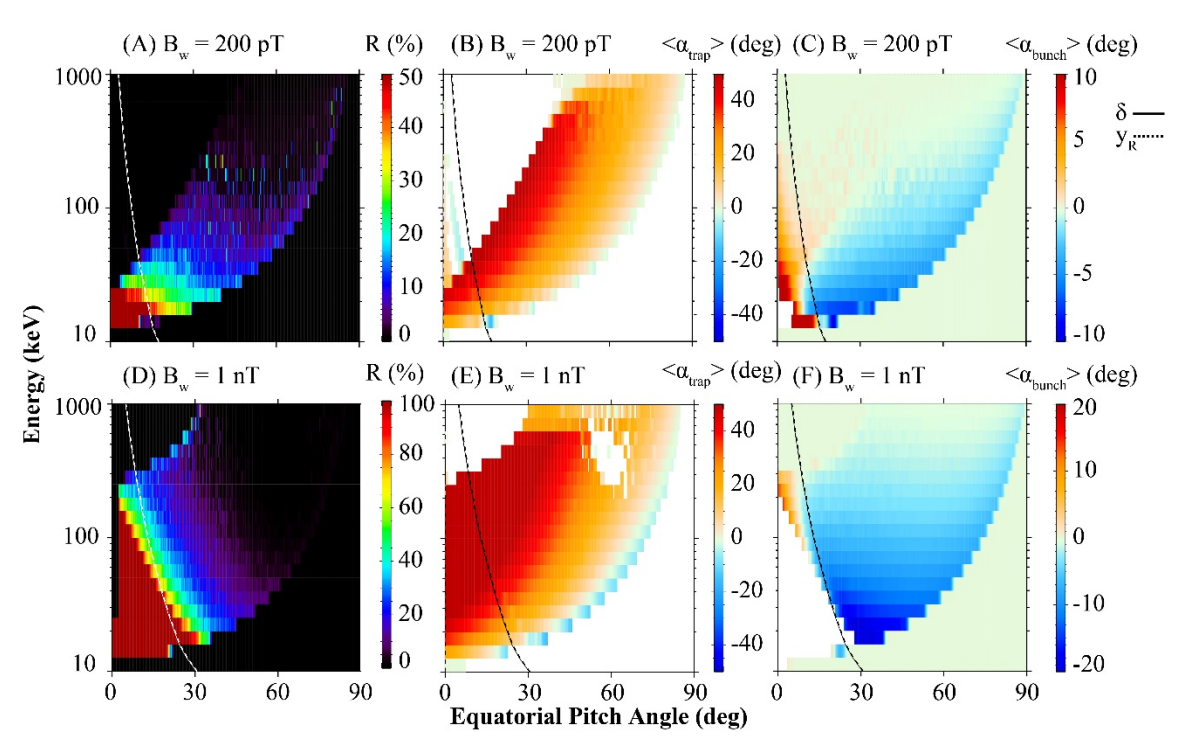
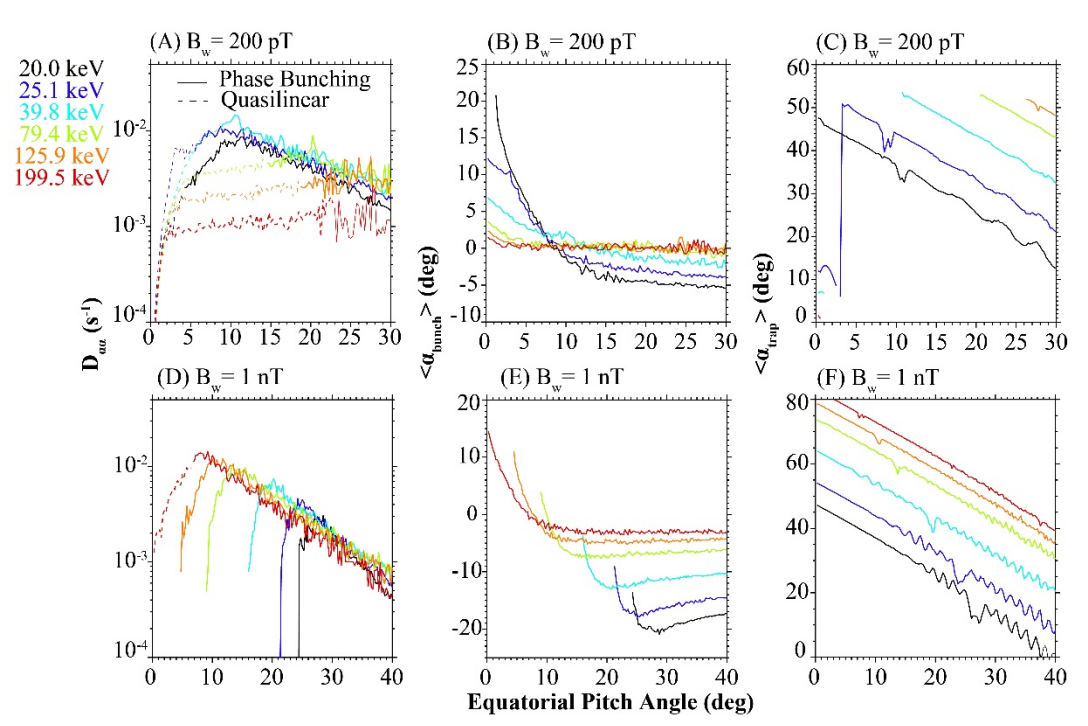


Figure 6. Phase trapping ratio and advection coefficients of both phase trapping and bunching distribution in equatorial pitch angle-energy space. (A) Phase trapping ratio; (B) advection coefficients of phase trapping electrons; (C) advection coefficients of phase bunching electrons for the amplitude of 200 pT. (D-F) Same as (A-C) but for the amplitude of 1 nT. Solid and dashed lines mark the theoretically calculated phase bunching boundary based on Albert et al. (2021) and Artemyev et al. (2021), respectively.

In Figure 7, we show the diffusion coefficients and advection coefficients of nonlinear processes with color coded lines for different energies to present their characteristics more clearly. Diffusion coefficients of phase bunching electrons for the wave amplitude of 200 pT are shown in Figure 7A in solid lines. As is shown in Figure 5C, for the amplitude of 200 pT, wave-particle interactions transit to the quasilinear regime as the electron pitch angle decreases and energy increases. We also show quasilinear diffusion coefficients of this region with dotted lines in Figure 7A for completeness, as phase bunching is not possible within the quasilinear regime. Pitch angle diffusion coefficients, shown in logarithmic scale, mostly decrease linearly as pitch angle increases. For nonlinear energy range (<40 keV), diffusion coefficients have similar values for a specific pitch angle, with the nonlinear pitch angle range extending to smaller pitch angles for lower energies. For higher energies, the quasilinear process is dominant. Quasilinear diffusion coefficients increase with pitch angle and decrease with energy. Such reverse in energy dependence corresponds to the flux ratio distribution versus energy shown in Figure 4A. The flux ratio also increases with energy in the nonlinear regime and decreases in the quasilinear regime for amplitude of 200 pT. Advection coefficients of phase bunching electrons (200 pT) are shown in Figure 7B. For energies within the nonlinear regime, phase bunching shows positive advection for small pitch angles and negative advection for larger pitch angles. The absolute values of phase bunching advection coefficients decrease with increasing energy. For quasilinear energies (above 40 keV), close-to-zero advection is shown due to the dominant diffusion process. Advection coefficients of phase trapping electrons are presented in Figure 7C, and they increase with increasing energy, as discussed above. Results of the amplitude of 1 nT are shown in the same format in Figures 7D-7F. In this case, all energies shown are in the nonlinear regime. Phase bunching diffusion coefficients of 1 nT for energies also follow the same trend, except for the pitch angle range close to the inner-most phase bunching boundary. Maximum diffusion coefficients also increase with increasing energy similar to what is shown in Figure 7A for the amplitude of 200 pT, but for all energies. Advection coefficients of phase bunching electrons decrease with increasing energy in the case of 1 nT. For lower energy electrons (< 40 keV), only negative phase bunching advection is observed. For higher energies, advection is positive at small pitch angles, and negative at larger pitch angles. Advection coefficients of trapping electrons exhibit a similar pitch angle distribution and increase with increasing energy.



429

430

431

432 433

434

435

436 437

438

439

440

441

442

443

444

445 446

447

448

449

450

451

452

453

454 455

456

459 **Figure 7.** Diffusion coefficients and advection coefficients of phase bunching and trapping electrons.

(A) Diffusion coefficients of phase bunching electrons interacting with the wave amplitude of 200 pT

shown in solid lines, color coded for different energies. The dashed lines show the quasilinear 461

diffusion coefficients in the quasilinear regime, where phase bunching is not possible. (B) Advection 462

463 coefficients of phase bunching electrons; (C) advection coefficients of phase trapping electrons. (D-

464 F) Same as (A-C) but for the amplitude of 1 nT.

4 **Discussions**

466 As discussed above, the precipitation flux ratio transits from nonlinear characteristics at low energies 467 to quasilinear characteristics at high energies, when the wave amplitude is 200 pT. For the amplitude of 1 nT, however, nonlinear characteristics persist for all resonant energies. The distribution of such

468 nonlinear characteristics can be quantitatively analyzed through the nonlinear inhomogeneity ratio. In

469 470

Figures 8A and 8B, we show the distribution of inhomogeneity ratio S, which follows Omura et al.

471 (2007):

460

465

$$S = \frac{1}{2\omega_t^2 \delta_*^2} \left\{ \left[\left(2 + \delta_*^2 \frac{\Omega_e - \gamma \omega}{\Omega_e - \omega} \right) V_R - \frac{k \gamma v_\perp^2}{\Omega_e} \right] \frac{\partial \Omega_e}{\partial h} \right\}$$
 (10)

473 Here, $\omega = 0.3 \Omega_{e0}$, v_{\perp} is the perpendicular electron velocity, and the definition of other parameters 474 can be found in Equation (1-11) in Omura et al. (2007). It is worth noting that δ_* is marked as δ in 475 Omura et al. (2007). A different notation is applied here to avoid confusion with Equation (6). The 476 criterion of |S| < 1 characterizes the nonlinear regime. The boundaries of nonlinear regimes defined 477 by |S| = 1 are marked with black solid lines in Figures 8A and 8B, corresponding to amplitudes of 200 pT and 1 nT. Within the nonlinear regime, $\delta = 0$ and $y_R = 1$ define the phase bunching 478 479 boundary, which are represented by white solid and dashed lines in Figure 8. Nonlinear boundary and 480 phase bunching boundary collectively define three regimes of different wave-particle interaction 481 characteristics that are related to electron precipitation. The distributions of these three regimes are 482 shown in Figures 8C and 8D for the amplitudes of 200 pT and 1 nT, respectively. Quasilinear regime, 483 where only electrons very close to the loss cone are scattered into it and precipitated, is marked by 484 green regions in Figure 8C. The red regions in these two panels mark the regime where electrons 485 interact with whistler-mode waves through anomalous scattering. The blue regions mark the region 486 where electrons undergo nonlinear phase trapping and phase bunching processes. As shown in Figure 487 8C, for the amplitude of 200 pT and energy below ~40 keV, anomalous trapping and positive 488 bunching transport electrons away from the loss cone and phase bunching dominates electron 489 precipitation process. For energy above 40 keV, quasilinear diffusion drives the electron precipitation 490 as the phase bunching boundary shifts closer to the loss cone. Such transition of driving mechanisms 491 for precipitation at energy of 40 keV explains the flux ratio distribution shown in Figure 4A, which 492 converges to quasilinear theory for energy above ~40 keV. For the amplitude of 1 nT, anomalous 493 trapping remains as the dominant wave-particle interaction for small pitch angles in the entire 494 resonant energy range. Thus, phase bunching drives electron precipitation for all resonant energies. 495 This corresponds to the nonlinear flux ratio for all energies, as shown in Figure 4A for the amplitude 496 of 1 nT.

497 As shown in Figures 8A and 8B, the inhomogeneity ratio S is not calculated for small pitch angle 498

regions, i.e., within the phase bunching boundary, which results in the gaps. This is because the

499 inhomogeneity ratio S from Omura et al. (2007) is not suitable for analyzing electrons with very

500 small equatorial pitch angles. The inhomogeneity ratio S is derived from Equation (5) of Omura et al. 501 (2007): $\frac{d\zeta}{dt} = k(v_{\parallel} - V_{R})$, where ζ is the relative phase between electron perpendicular velocity and 502 wave magnetic field vector, v_{\parallel} is the parallel velocity of electrons, and $V_{R} = (\omega - \Omega_{e}/\gamma)/k$ is the 503 resonance velocity. For small pitch angles, this simplified equation of phase variation is not accurate 504 and a full version needs to be applied (Kitahara & Katoh, 2019):

$$\frac{d\zeta}{dt} = k(v_{\parallel} - V_{R}) + \frac{e(E_{w} - v_{\parallel}B_{W})}{m\gamma v_{\perp}} \cos\zeta \tag{11}$$

Here, e is the electron charge, m is the electron mass, E_w and B_w are the wave electric and magnetic 506 507 field respectively. The second term in Equation (11) becomes comparable to or even much larger than the first term when electron pitch angle is small and thus cannot be dropped out of the equation. 508 509 This complication at the small electron pitch angle requires the derivation of a new form of 510 inhomogeneity for the electron precipitation scenario. Albert et al. (2021) presented parameters R_0 , R_2 , and R_3 which generalize the inhomogeneity parameter for small pitch angles regions. This is, 511 however, not the focus of this paper and is left as future work. Although the current inhomogeneity is 512 513 not applicable to the left of the phase bunching boundary (white lines), it is applicable to the right of 514 it, when the second term in Equation (11) becomes much smaller than the first term. Thus, the 515 transition energy determined from intersection between the black and white lines is still qualitatively 516 valid. In conclusion, by combining the current version of inhomogeneity ratio and bunching 517 boundary, we can roughly estimate the energy at which precipitation transits from nonlinear to quasilinear characteristics, which increases with increasing wave amplitude. However, a more 518 accurate expression for inhomogeneity ratio is still crucial for accurate quantification of the nonlinear 519 520 precipitation regime.

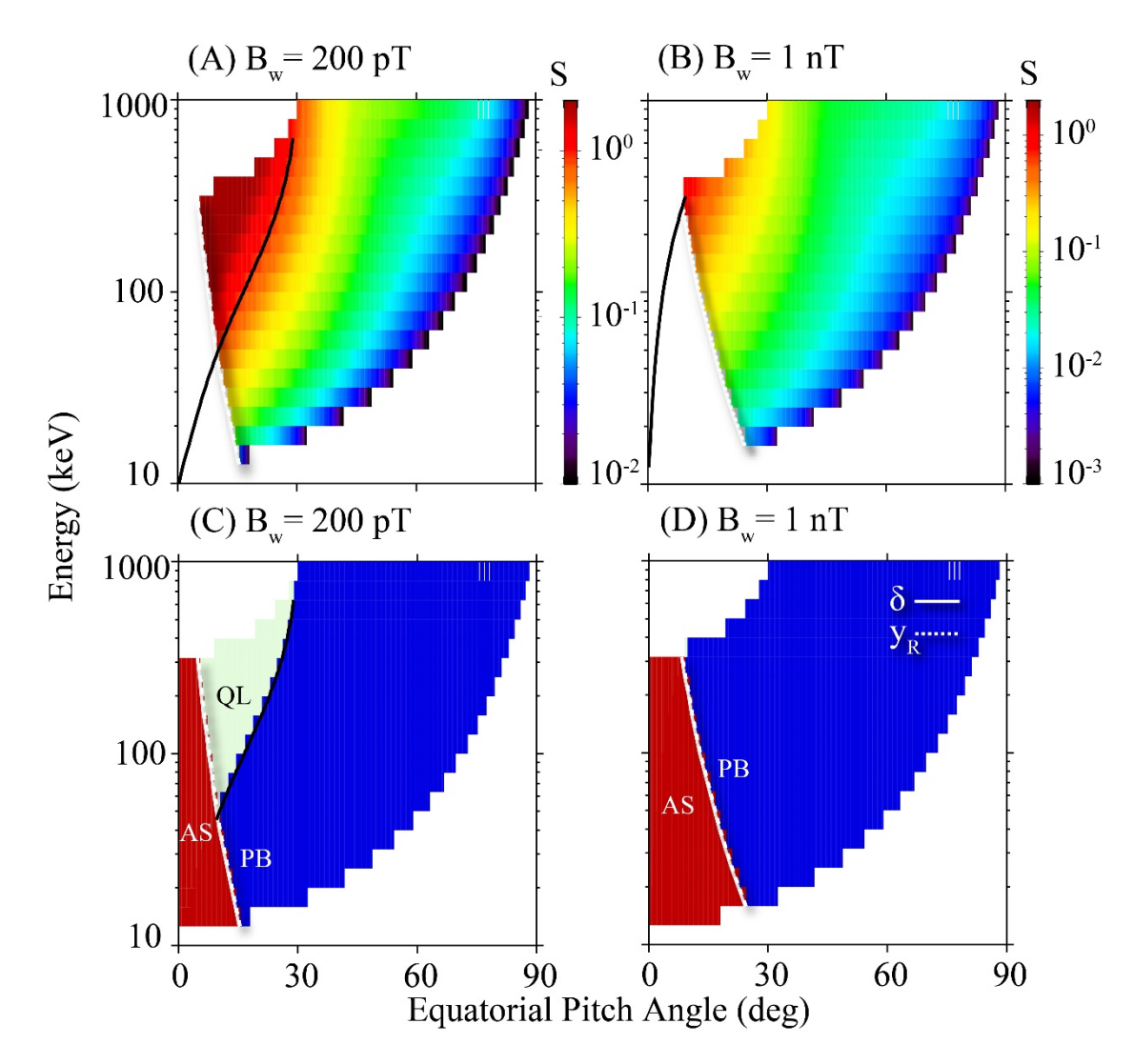


Figure 8. The distribution of inhomogeneity ratio and different regimes in electron equatorial pitch angle-energy space. (A) Inhomogeneity ratio (S) distribution for the amplitude of 200 pT. Black solid line marks the points where S=1. The white solid and dashed lines mark the theoretically derived phase bunching boundary from Albert et al. (2021) and Artemyev et al. (2021). (B) Inhomogeneity ratio S distribution for the amplitude of 1 nT. (C) Distribution of different regimes in pitch angle-energy space for the amplitude of 200 pT. Green region represents quasilinear regime, where electrons are diffused into the loss cone via quasilinear processes. Red region marks the region where electrons are anomalously trapped or positively bunched away from the loss cone. Blue region marks the region where electrons can be precipitated through phase bunching processes. (D) Same as (C) but for the amplitude of 1 nT.

The simulations in this paper assume a uniform wave amplitude, which may be approximated by a very long wave packet. As shown by Zhang et al. (2019), short and intense whistler-mode wave packets are also commonly observed in the Earth's radiation belts. These short packets are able to resonate with electrons nonlinearly, but would significantly reduce the trapping effects, including the anomalous trapping (Artemyev, Neishtadt, Vasiliev, et al., 2021; Gan et al., 2020; Mourenas et al., 2018). This may lead to a more diffusive precipitation process, which was discussed in Mourenas et al. (2022). The effects of wave packet length, and the wave coherency (Zhang et al., 2020) need to be considered in the numerical simulations and are left as future extensions of this paper.

540 5 Conclusions

- In this paper, we systematically estimate the combined effects of anomalous scattering and phase
- bunching caused by intense whistler-mode waves on electron precipitation. We proposed a new
- 543 physical picture of energetic electron precipitation in the nonlinear regime. The transition of electron
- 544 precipitation from quasilinear to nonlinear regimes is analyzed using current theories. Nonlinear
- diffusion and advection coefficients, which are crucial for the nonlinear precipitation processes, are
- also calculated using the test particle simulations. The key findings of this paper are summarized
- 547 below:
- Nonlinear electron precipitation is driven by phase bunching right outside the phase bunching boundary, instead of right outside of the loss cone.
- Anomalous trapping and positive phase bunching prevent electrons within the phase bunching boundary from precipitation.
- Nonlinear precipitation region is determined by both the phase bunching boundary and inhomogeneity ratio and is dominant at lower energies. The maximum energy for nonlinear precipitation increases with increasing wave amplitude.
- Phase bunching driven precipitation leads to a smaller flux ratio compared to quasilinear expectations at the quasi-equilibrium state.
- 557 5. Maximum phase bunching diffusion coefficients are much smaller than those from quasilinear theory. Phase bunching diffusion coefficients near the phase bunching boundary increase with increasing energy.
- The results from this study are based on purely parallel whistler-mode waves. Previous studies have
- also shown abundant large amplitude oblique whistler-mode waves with wave normal angles close to
- the resonance cone angle (e.g., Cattell et al., 2008; Li et al., 2016). The nonlinear effects for these
- quasi-electrostatic whistler-mode waves can be very different from parallel waves (Artemyev et al.,
- 564 2013; Goyal et al., 2017; Zhang, Artemyev, et al., 2022) and further investigation is needed to fully
- understand their roles in electron precipitation.
- 566 Determination of phase bunching boundary is crucial to understanding precipitation in the nonlinear
- regime. Previous theoretical analyses have provided rough estimates of this boundary. However,
- these theoretical analyses are focused on anomalous trapping and do not consider positive bunching
- process. Thus, the theoretical results do not agree with the numerical results well for the case of 200
- pT where positive bunching also plays a significant role. Further numerical and theoretical studies
- that quantitatively determine the phase bunching are important and left as future work.
- As shown in this paper, the pitch angle distribution of precipitation PSD is different from quasilinear
- expectations in the nonlinear regime, which leads to a smaller flux ratio. This could be due to the fact
- that phase bunching diffusion coefficients near the phase bunching boundary is much smaller than
- 575 quasilinear diffusion coefficients near the loss cone. Theoretical expressions of the nonlinear
- 576 precipitation PSD distribution using nonlinear diffusion and advection coefficients could serve as an
- interesting future study. Potential results from these future studies could also contribute to improving
- 578 the method of calculating whistler-mode wave intensity based on the electron precipitation ratio
- proposed by Li et al. (2013), which relies on quasilinear theory (Kennel & Petschek, 1966). It is also
- important to evaluate the relative contributions of the advection and diffusion coefficients in driving
- the electron precipitation, as well as determine the precipitation to trapped flux ratio. If the phase
- bunching advection coefficients are the dominant term, the precipitation ratio will be more sensitive
- to the electron pitch angle distribution and the large pitch angle gradient of the PSD near the phase

584 585 586 587 588 589	bunching boundary could potentially lead to local peaks or an inverse PSD gradient within the loss cone. On the other hand, if phase bunching diffusion coefficients are dominant, the electron pitch angle distribution near the loss cone are not sensitive to the electron pitch angle distribution, similar to what was predicted by the quasilinear theory (e.g., Kennel and Petschek, 1966), although the distribution would be different from the quasilinear prediction due to the different diffusion coefficients from phase bunching, as discussed above.
590 591 592 593 594 595 596	Inhomogeneity ratio has been commonly used to estimate the nonlinear effects of whistler-mode waves. However, as discussed in this paper, previous analytical expressions of the inhomogeneity ratio are not applicable concerning the precipitation problem, since the electron pitch angle is small and major assumptions of the derivation of these inhomogeneity ratios become invalid. Further studies on the correct form of inhomogeneity ratio at very small pitch angles are essential to our understanding of the role of nonlinear interactions in electron precipitation. This is beyond the scope of this paper and is left as a follow-up study.
597	6 Author Contributions
598 599 600 601 602	The first author, LG, is responsible for producing the main results of this manuscript, including numerical simulations and theoretical analyses. LG is also the writer of this manuscript. WL provides key suggestions and guidance in the entire process of this study, as well as comments and suggestions to the final manuscript. MH, QM, JA, and AA all provided valuable theoretical and numerical discussions and suggestions.
603	7 Funding
604 605 606 607	At Boston University, this research is supported by NASA grants 80NSSC20K0698, 80NSSC19K0845, 80NSSC21K1312, and 80NSSC20K0196, NSF grants AGS-1847818, AGS-2019950, and AGS-2225445. LG gratefully acknowledges the NASA FINESST grant 80NSSC20K1506.
608	8 References
609	Albert, J. M. (2000). Gyroresonant interactions of radiation belt particles with a monochromatic
610	electromagnetic wave. Journal of Geophysical Research: Space Physics, 105(A9), 21191-
611	21209. https://doi.org/10.1029/2000JA000008
612	Albert, J. M., Artemyev, A. V., Li, W., Gan, L., & Ma, Q. (2021). Models of Resonant Wave-Particle
613	Interactions. Journal of Geophysical Research: Space Physics, 126(6), e2021JA029216.
614	https://doi.org/10.1029/2021JA029216
615	Albert, Jay M. (1993). Cyclotron resonance in an inhomogeneous magnetic field. <i>Physics of Fluids</i>
616	B: Plasma Physics, 5(8), 2744–2750. https://doi.org/10.1063/1.860715

617	Albert, Jay M., Meredith, N. P., & Horne, R. B. (2009). Three-dimensional diffusion simulation of
618	outer radiation belt electrons during the 9 October 1990 magnetic storm. Journal of
619	Geophysical Research: Space Physics, 114(A9). https://doi.org/10.1029/2009JA014336
620	Artemyev, A. V., Vasiliev, A. A., Mourenas, D., Agapitov, O. V., & Krasnoselskikh, V. V. (2013).
621	Nonlinear electron acceleration by oblique whistler waves: Landau resonance vs. cyclotron
622	resonance. Physics of Plasmas, 20(12), 122901. https://doi.org/10.1063/1.4836595
623	Artemyev, A. V., Vasiliev, A. A., Mourenas, D., Agapitov, O. V., Krasnoselskikh, V., Boscher, D.,
624	& Rolland, G. (2014). Fast transport of resonant electrons in phase space due to nonlinear
625	trapping by whistler waves. Geophysical Research Letters, 41(16), 5727-5733.
626	https://doi.org/10.1002/2014GL061380
627	Artemyev, A. V., Neishtadt, A. I., Vainchtein, D. L., Vasiliev, A. A., Vasko, I. Y., & Zelenyi, L. M.
628	(2018). Trapping (capture) into resonance and scattering on resonance: Summary of results
629	for space plasma systems. Communications in Nonlinear Science and Numerical Simulations,
630	65, 111–160. https://doi.org/10.1016/j.cnsns.2018.05.004
631	Artemyev, A. V., Neishtadt, A. I., Albert, J. M., Gan, L., Li, W., & Ma, Q. (2021). Theoretical model
632	of the nonlinear resonant interaction of whistler-mode waves and field-aligned electrons.
633	Physics of Plasmas, 28(5), 052902. https://doi.org/10.1063/5.0046635
634	Artemyev, A. V., Neishtadt, A. I., Vasiliev, A. A., & Mourenas, D. (2021). Transitional regime of
635	electron resonant interaction with whistler-mode waves in inhomogeneous space plasma.
636	Physical Review E, 104(5), 055203. https://doi.org/10.1103/PhysRevE.104.055203
637	Bellan, P. M. (2013). Pitch angle scattering of an energetic magnetized particle by a circularly
638	polarized electromagnetic wave. Physics of Plasmas, 20(4), 042117.
639	https://doi.org/10.1063/1.4801055

640 Blake, J. B., Looper, M. D., Baker, D. N., Nakamura, R., Klecker, B., & Hovestadt, D. (1996). New 641 high temporal and spatial resolution measurements by SAMPEX of the precipitation of 642 relativistic electrons. Advances in Space Research, 18(8), 171–186. 643 https://doi.org/10.1016/0273-1177(95)00969-8 644 Bortnik, J., Thorne, R. M., & Inan, U. S. (2008). Nonlinear interaction of energetic electrons with 645 large amplitude chorus. Geophysical Research Letters, 35(21). 646 https://doi.org/10.1029/2008GL035500 647 Bortnik, Jacob, Albert, J. M., Artemyev, A., Li, W., Jun, C.-W., Grach, V. S., & Demekhov, A. G. 648 (2022). Amplitude Dependence of Nonlinear Precipitation Blocking of Relativistic Electrons 649 by Large Amplitude EMIC Waves. Geophysical Research Letters, 49(12), e2022GL098365. 650 https://doi.org/10.1029/2022GL098365 651 Breneman, A. W., Crew, A., Sample, J., Klumpar, D., Johnson, A., Agapitov, O., et al. (2017). 652 Observations Directly Linking Relativistic Electron Microbursts to Whistler Mode Chorus: Van Allen Probes and FIREBIRD II. Geophysical Research Letters, 44(22), 11,265-11,272. 653 654 https://doi.org/10.1002/2017GL075001 655 Cattell, C., Wygant, J. R., Goetz, K., Kersten, K., Kellogg, P. J., Rosenvinge, T. von, et al. (2008). 656 Discovery of very large amplitude whistler-mode waves in Earth's radiation belts. 657 Geophysical Research Letters, 35(1). https://doi.org/10.1029/2007GL032009 658 Chen, L., Zhang, X.-J., Artemyev, A., Angelopoulos, V., Tsai, E., Wilkins, C., & Horne, R. B. 659 (2022). Ducted Chorus Waves Cause Sub-Relativistic and Relativistic Electron Microbursts. 660 Geophysical Research Letters, 49(5), e2021GL097559. 661 https://doi.org/10.1029/2021GL097559

002	Denion, R. E., Menietti, J. D., Goldstein, J., Young, S. L., & Anderson, R. R. (2004). Electron
663	density in the magnetosphere. Journal of Geophysical Research: Space Physics, 109(A9).
664	https://doi.org/10.1029/2003JA010245
665	Douma, E., Rodger, C. J., Clilverd, M. A., Hendry, A. T., Engebretson, M. J., & Lessard, M. R.
666	(2018). Comparison of Relativistic Microburst Activity Seen by SAMPEX With Ground-
667	Based Wave Measurements at Halley, Antarctica. Journal of Geophysical Research: Space
668	Physics, 123(2), 1279–1294. https://doi.org/10.1002/2017JA024754
669	Frantsuzov, V. A., Artemyev, A. V., Zhang, XJ., Allanson, O., Shustov, P. I., & Petrukovich, A. A.
670	(2023). Diffusive scattering of energetic electrons by intense whistler-mode waves in an
671	inhomogeneous plasma. Journal of Plasma Physics, 89(1), 905890101.
672	https://doi.org/10.1017/S0022377822001271
673	Gan, L., Li, W., Ma, Q., Albert, J. M., Artemyev, A. V., & Bortnik, J. (2020). Nonlinear Interactions
674	Between Radiation Belt Electrons and Chorus Waves: Dependence on Wave Amplitude
675	Modulation. Geophysical Research Letters, 47(4), e2019GL085987.
676	https://doi.org/10.1029/2019GL085987
677	Goyal, R., Sharma, R. P., & Kumar, S. (2017). Nonlinear effects associated with quasi-electrostatic
678	whistler waves relevant to that in radiation belts. Journal of Geophysical Research: Space
679	Physics, 122(1), 340-348. https://doi.org/10.1002/2016JA023274
680	Grach, V. S., & Demekhov, A. G. (2020). Precipitation of Relativistic Electrons Under Resonant
681	Interaction With Electromagnetic Ion Cyclotron Wave Packets. Journal of Geophysical
682	Research: Space Physics, 125(2), e2019JA027358. https://doi.org/10.1029/2019JA027358
683	Grach, Veronika S., Artemyev, A. V., Demekhov, A. G., Zhang, XJ., Bortnik, J., Angelopoulos, V.
684	et al. (2022). Relativistic Electron Precipitation by EMIC Waves: Importance of Nonlinear

685 Resonant Effects. Geophysical Research Letters, 49(17), e2022GL099994. 686 https://doi.org/10.1029/2022GL099994 687 Hanzelka, M., Li, W., & Ma, Q. (2023). Parametric analysis of pitch angle scattering and losses of 688 relativistic electrons by oblique EMIC waves. Frontiers in Astronomy and Space Sciences, 689 10. Retrieved from https://www.frontiersin.org/articles/10.3389/fspas.2023.1163515 690 Henrard, J., & Lemaitre, A. (1983). A second fundamental model for resonance. Celestial Mechanics, 691 30(2), 197–218. https://doi.org/10.1007/BF01234306 692 Horne, R. B., Thorne, R. M., Glauert, S. A., Albert, J. M., Meredith, N. P., & Anderson, R. R. 693 (2005). Timescale for radiation belt electron acceleration by whistler mode chorus waves. 694 Journal of Geophysical Research: Space Physics, 110(A3). 695 https://doi.org/10.1029/2004JA010811 696 Kennel, C. F., & Engelmann, F. (1966). Velocity Space Diffusion from Weak Plasma Turbulence in 697 a Magnetic Field. The Physics of Fluids, 9(12), 2377–2388. 698 https://doi.org/10.1063/1.1761629 699 Kennel, C. F., & Petschek, H. E. (1966). Limit on stably trapped particle fluxes. *Journal of* 700 Geophysical Research (1896-1977), 71(1), 1–28. https://doi.org/10.1029/JZ071i001p00001 701 Kitahara, M., & Katoh, Y. (2019). Anomalous Trapping of Low Pitch Angle Electrons by Coherent 702 Whistler Mode Waves. Journal of Geophysical Research: Space Physics, 124(7), 5568–5583. 703 https://doi.org/10.1029/2019JA026493 704 Li, W., Ni, B., Thorne, R. M., Bortnik, J., Green, J. C., Kletzing, C. A., et al. (2013). Constructing the 705 global distribution of chorus wave intensity using measurements of electrons by the POES 706 satellites and waves by the Van Allen Probes. Geophysical Research Letters, 40(17), 4526— 707 4532. https://doi.org/10.1002/grl.50920

708 Li, W., Thorne, R. M., Ma, Q., Ni, B., Bortnik, J., Baker, D. N., et al. (2014). Radiation belt electron 709 acceleration by chorus waves during the 17 March 2013 storm. Journal of Geophysical 710 Research: Space Physics, 119(6), 4681–4693. https://doi.org/10.1002/2014JA019945 711 Li, W., Santolik, O., Bortnik, J., Thorne, R. M., Kletzing, C. A., Kurth, W. S., & Hospodarsky, G. B. 712 (2016). New chorus wave properties near the equator from Van Allen Probes wave 713 observations. Geophysical Research Letters, 43(10), 4725–4735. 714 https://doi.org/10.1002/2016GL068780 715 Lyons, L. R. (1974). Pitch angle and energy diffusion coefficients from resonant interactions with 716 ion-cyclotron and whistler waves. Journal of Plasma Physics, 12(3), 417–432. 717 https://doi.org/10.1017/S002237780002537X 718 Ma, Q., Li, W., Bortnik, J., Thorne, R. M., Chu, X., Ozeke, L. G., et al. (2018). Quantitative 719 Evaluation of Radial Diffusion and Local Acceleration Processes During GEM Challenge 720 Events. Journal of Geophysical Research: Space Physics, 123(3), 1938–1952. 721 https://doi.org/10.1002/2017JA025114 722 Miyoshi, Y., Saito, S., Kurita, S., Asamura, K., Hosokawa, K., Sakanoi, T., et al. (2020). Relativistic 723 Electron Microbursts as High-Energy Tail of Pulsating Aurora Electrons. Geophysical 724 Research Letters, 47, e90360. https://doi.org/10.1029/2020GL090360 725 Mourenas, D., Zhang, X.-J., Artemyev, A. V., Angelopoulos, V., Thorne, R. M., Bortnik, J., et al. 726 (2018). Electron Nonlinear Resonant Interaction With Short and Intense Parallel Chorus 727 Wave Packets. Journal of Geophysical Research: Space Physics, 123(6), 4979–4999. 728 https://doi.org/10.1029/2018JA025417 729 Mourenas, D., Zhang, X.-J., Nunn, D., Artemyev, A. V., Angelopoulos, V., Tsai, E., & Wilkins, C.

(2022). Short Chorus Wave Packets: Generation Within Chorus Elements, Statistics, and

/31	Consequences on Energetic Electron Precipitation. Journal of Geophysical Research: Space
732	Physics, 127(5), e2022JA030310. https://doi.org/10.1029/2022JA030310
733	Mozer, F. S., Agapitov, O. V., Blake, J. B., & Vasko, I. Y. (2018). Simultaneous Observations of
734	Lower Band Chorus Emissions at the Equator and Microburst Precipitating Electrons in the
735	Ionosphere. Geophysical Research Letters, 45(2), 511–516.
736	https://doi.org/10.1002/2017GL076120
737	Neishtadt, A. I. (1975). Passage through a separatrix in a resonance problem with a slowly-varying
738	parameter: PMM vol. 39, n≗ 4, 1975, pp. 621–632. Journal of Applied Mathematics and
739	Mechanics, 39(4), 594-605. https://doi.org/10.1016/0021-8928(75)90060-X
740	Nunn, D., & Omura, Y. (2015). A computational and theoretical investigation of nonlinear wave-
741	particle interactions in oblique whistlers. Journal of Geophysical Research (Space Physics),
742	120(4), 2890–2911. https://doi.org/10.1002/2014JA020898
743	O'Brien, T. P., Looper, M. D., & Blake, J. B. (2004). Quantification of relativistic electron
744	microburst losses during the GEM storms. Geophysical Research Letters, 31(4).
745	https://doi.org/10.1029/2003GL018621
746	Omura, Y., Furuya, N., & Summers, D. (2007). Relativistic turning acceleration of resonant electrons
747	by coherent whistler mode waves in a dipole magnetic field. Journal of Geophysical
748	Research: Space Physics, 112(A6). https://doi.org/10.1029/2006JA012243
749	Shumko, M., Turner, D. L., O'Brien, T. P., Claudepierre, S. G., Sample, J., Hartley, D. P., et al.
750	(2018). Evidence of Microbursts Observed Near the Equatorial Plane in the Outer Van Allen
751	Radiation Belt. Geophysical Research Letters, 45(16), 8044–8053.
752	https://doi.org/10.1029/2018GL078451

- 753 Tao, X., & Bortnik, J. (2010). Nonlinear interactions between relativistic radiation belt electrons and
- oblique whistler mode waves. *Nonlinear Processes in Geophysics*, 17(5), 599–604.
- 755 https://doi.org/10.5194/npg-17-599-2010
- 756 Thorne, R. M., O'Brien, T. P., Shprits, Y. Y., Summers, D., & Horne, R. B. (2005). Timescale for
- 757 MeV electron microburst loss during geomagnetic storms. *Journal of Geophysical Research*:
- 758 Space Physics, 110(A9). https://doi.org/10.1029/2004JA010882
- 759 Thorne, R. M., Li, W., Ni, B., Ma, Q., Bortnik, J., Chen, L., et al. (2013). Rapid local acceleration of
- relativistic radiation-belt electrons by magnetospheric chorus. *Nature*, 504(7480), 411–414.
- 761 https://doi.org/10.1038/nature12889
- Vainchtein, D., Zhang, X.-J., Artemyev, A. V., Mourenas, D., Angelopoulos, V., & Thorne, R. M.
- 763 (2018). Evolution of Electron Distribution Driven by Nonlinear Resonances With Intense
- Field-Aligned Chorus Waves. Journal of Geophysical Research (Space Physics), 123(10),
- 765 8149–8169. https://doi.org/10.1029/2018JA025654
- 766 Zhang, X.-J., Thorne, R., Artemyev, A., Mourenas, D., Angelopoulos, V., Bortnik, J., et al. (2018).
- Properties of Intense Field-Aligned Lower-Band Chorus Waves: Implications for Nonlinear
- Wave-Particle Interactions. Journal of Geophysical Research (Space Physics), 123(7), 5379–
- 769 5393. https://doi.org/10.1029/2018JA025390
- Zhang, X. -J., Mourenas, D., Artemyev, A. V., Angelopoulos, V., Bortnik, J., Thorne, R. M., et al.
- 771 (2019). Nonlinear Electron Interaction With Intense Chorus Waves: Statistics of Occurrence
- 772 Rates. \(\gamma rl, 46(13)\), 7182–7190. https://doi.org/10.1029/2019GL083833
- 773 Zhang, Xiao-Jia, Angelopoulos, V., Mourenas, D., Artemyev, A., Tsai, E., & Wilkins, C. (2022).
- 774 Characteristics of Electron Microburst Precipitation Based on High-Resolution ELFIN

7/5	Measurements. Journal of Geophysical Research: Space Physics, 12/(5), e2022JA030509.
776	https://doi.org/10.1029/2022JA030509
777	Zhang, Xiao-Jia, Artemyev, A., Angelopoulos, V., Tsai, E., Wilkins, C., Kasahara, S., et al. (2022).
778	Superfast precipitation of energetic electrons in the radiation belts of the Earth. Nature
779	Communications, 13(1), 1611. https://doi.org/10.1038/s41467-022-29291-8
780	Zhang, XJ., Agapitov, O., Artemyev, A. V., Mourenas, D., Angelopoulos, V., Kurth, W. S., et al.
781	(2020). Phase Decoherence Within Intense Chorus Wave Packets Constrains the Efficiency of
782	Nonlinear Resonant Electron Acceleration. Geophysical Research Letters, 47(20),
783	e2020GL089807. https://doi.org/10.1029/2020GL089807
784	
785	12 Data Availability Statement
786	The datasets for this study can be found in 10.6084/m9.figshare.23282702.